Binary ZnS–ZnO films as an alternative buffer layer for solar cell applications

Olcay Gençyılmaz[1] · İdris Akyüz[2] · Ferhunde Atay[2]

Abstract

In this research, binary ZnS–ZnO films were fabricated by a two-step process, offering an alternative buffer layer solution for photovoltaic solar cell applications. ZnS films were attained through thermal evaporation, after which they were annealed in air at separate temperatures resulting in films containing both ZnS and ZnO phases. Structural, electrical, ellipsometric, optical, and surface properties were examined in detail to elucidate their applicability as a buffer layer in photovoltaic applications. X-ray diffraction patterns revealed that the films exhibit cubic ZnS and hexagonal ZnO crystal structures, wherein crystallite size is augmented with higher annealing temperatures. ZnS films exhibited a needle-shaped surface morphology, as confirmed through atomic force microscopy (AFM) and field emission scanning electron microscopy (FESEM) images. Annealing caused noteworthy modifications on the surfaces of the films. Additionally, absorption spectra denote two distinct absorption regions forming as a result of the annealing process, possibly indicating the emergence of ZnS and ZnO phases. Photoluminescence analyses demonstrate that binary ZnS–ZnO films exhibit greater emission intensities than single-phase ZnS films. Additionally, the annealing process caused the electrical resistivity of films to reduce from 1.28×10^5 to 3.84×10^1 Ω cm. These results suggest that binary ZnS–ZnO films produced via annealing can be considered as promising buffer layers in potential photovoltaic solar cell applications.

Keywords Solar cell · Buffer layer · ZnS-ZnO films · Thermal evaporation

1 Introduction

In recent years, the importance of investigating materials suitable for CIGS and CZTS heterojunction solar cell design and assessing their performance has increased. Researchers have extensively studied the properties of absorber, buffer, and transparent conductive oxide layers to enhance the device efficiency. When it comes to device efficiency, the role of the buffer layer between the transparent conductive oxide and the absorber layer is known as an important factor.

A suitable buffer layer must hinder e–h pair recombination between the front contact and the absorber layer. Thus, it is necessary to ensure that the buffer layer possesses a wide band gap in the visible region, high optical transmission, and appropriate electrical resistivity. CdS, ZnS, and ZnSe are examples of semiconductor thin films that are commonly used as buffer layer materials, and are compatible with CIGS and CZTS absorber layers [1, 2]. CdS is the most commonly employed buffer layer among these films. Nonetheless, its narrow band gap, toxic waste, and various intermediate state defects have led researchers to investigate new and alternative materials such as ZnS and ZnSe. ZnS semiconductor films typically have a band gap of 3.5–3.7 eV. For these values, the fundamental absorption range in the solar spectrum is approximately 335–355 nm, whereas the forbidden energy gap for CdS is roughly 2.5 eV, which corresponds to approximately 500 nm. Therefore, using an alternative ZnS material as a buffer layer may be a solution to photons that cannot be used in the visible region of the spectrum leading to the generation of more charge carriers and current [3]. In addition to their non-toxic nature, ZnS films are notable for their high transparency in the solar spectrum, fluorescence effect, and high refractive index (2.35) as well as their n/p-type electrical conductivity [3–12].

✉ Olcay Gençyılmaz
eren_o@hotmail.com

1 Department of Material and Material Proceeding Technologies, Çankırı Karatekin University, Çankırı, Turkey

2 Department of Physics, Eskişehir Osmangazi University, Eskişehir, Turkey

However, ZnS has significant drawbacks as a buffer layer, such as its lattice mismatch and high resistance [13, 14]. In recent years, solar cells have featured binary films which share similar crystal structures, lattice constants, and physical and chemical properties such as ZnS–ZnO to solve these types of problems. By creating a binary structure, films with varying physical properties can be produced. ZnS–ZnO binary films have been shown to form superior junctions compared to CdS by reducing interface recombination and providing optimal band alignment between the layers. It is also feasible to reduce the loss of photocurrent within the short wavelength region and boost conduction at the buffer/absorber junction by altering the stoichiometry of ZnS through thermal oxidation [15, 16].

Zinc sulfide (ZnS) films were synthesized via various physical and chemical methods, including chemical bath deposition [17], spray pyrolysis [18], successive ionic layer adsorption and reaction (SILAR) [19, 20], sol–gel synthesis [21, 22], thermal evaporation [23], and spraying [24]. Among these techniques, thermal evaporation has several benefits, such as ease of adjusting production parameters, reproducibility, and feasibility for large-scale surface production under vacuum conditions [25]. It has been previously shown that it is possible to control the absorption and photon emissions by the formation of the ZnS/ZnO structures, representing type-II band alignment [26, 27]. Also, there are theoretical studies reporting on promising advantage of band alignment modification by the formation of ZnS/ZnO structure [28]. Further benefits include the capacity to control thickness and achieve smooth surfaces and thin-layered constructions which are all critical processes for solar cell materials.

In this study, our main purpose is to create alternative ZnS based coatings that can serve as buffer layer in heterojunction solar cells through the thermal evaporation method. For this purpose, we have obtained alternative ZnS–ZnO buffer layers by applying thermal annealing process at different temperatures and examined the effect of dual nature (ZnS–ZnO) on the structural, optical, surface and electrical properties.

2 Experimental

2.1 Production of ZnS–ZnO films

In this study, ZnS films were produced onto microscope glass substrates (Objekttrager microscope slide) using PVD Handy 2 T Vacuum-Evaporation System. First of all, the glass substrates were washed separately for 20 min using deionized water in the ultrasonic bath and dried in the oven. Solid ZnS pieces (99.99%) with a density of 3.98 g/cm^3 were used as target to produce ZnS films. Deposition process was performed at a deposition rate of 5 Å/s by applying a current of 120 A to a tungsten boat. Thickness control was achieved with a quartz crystal sensor. To obtain ZnS–ZnO films, ZnS layers were annealed in air for 1 h at three different temperatures (425 °C, 475 °C, and 525 °C). The produced films were named as ZnS, ZnS-425, ZnS-475 and ZnS-525.

2.2 Characterization of ZnS–ZnO films

The structural, optical, surface, and electrical properties of ZnS–ZnO films were investigated by several analysis techniques in order to investigate their potential as a buffer layer in solar cells. In order to examine the structural properties of the films, X-ray diffraction (XRD) patterns were taken by Panalytical Empyrean X-ray diffractometer using CuK$_\alpha$ beam ($\lambda = 1.5406$ Å) in $20° \leq 2\theta \leq 80°$ range. The thickness values and optical constants [refractive index (n), and extinction coefficient (k)] of the films were determined using OPT-S9000 Spectroscopic Ellipsometer (*SE*). The transmittance (T), absorption (A) and reflection (R) spectra were taken using Shimadzu UV-2550 UV–Vis Spectrophotometer, and the optical band gaps (E_g) were calculated by optical method. To obtain information about point defects, photoluminescence spectra were taken using Perkin Elmer LS55 Fluorescence Spectrophotometer. Field Emission Scanning Electron Microscopy (*FESEM,* Hitachi Regulus 8230) was used to examine the surface properties of the films. In addition, chemical compositions were analyzed by Energy Dispersive X-ray Spectroscopy (EDX). Park Systems XE-100 atomic force microscope (AFM) was used to investigate surface morphologies, and average (R_a), rms (R_q), and peak-valley (R_{pv}) roughness values were determined by XEI version 1.7.1 software. Electrical resistivity values were determined by a two-probe technique using the Keithley 2400 SourceMeter and Keithley 6514 System Electrometer.

3 Results and discussions

3.1 Structural properties

The XRD patterns of ZnS–ZnO films are shown in Fig. 1. Besides, Table 1 gives the interplanar spacing (d), interplanar spacing without deformation (d_0), diffraction angles (2θ), Miller indices (hkl) and crystal systems for all films. As can be seen in Fig. 2, for all films, ZnS phase growth performed through (111) plane. On the other hand, for annealed films, an additional ZnO phase through (002) plane has emerged, showing the binary nature of ZnS–ZnO films. The preferential orientation of all films up to the annealing temperature of 525 °C is (111) ZnS at ~29°. For the annealed films, besides the (111)-ZnS phase, the ZnO phase in the direction of the (002) plane is also observed. With the increase in annealing
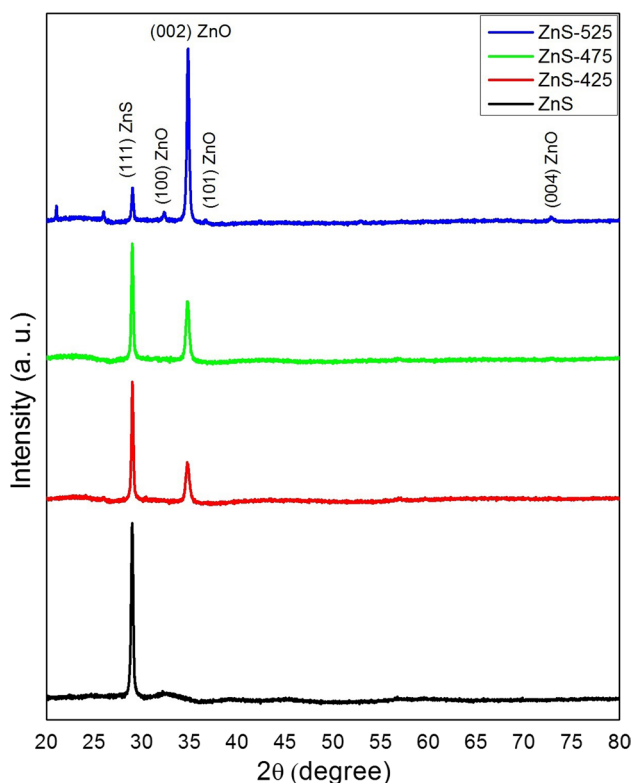
Fig. 1 X-ray diffraction patterns of ZnS–ZnO films

the annealing temperature is greater than 300 °C, sulfur and zinc in the structure react with the oxygen in the environment. In this case, while the S in the structure decreases, the Zn ion binds with O to form ZnO. This chemical reaction of the loss of sulfur resulting from oxidation at high temperatures is as follows [34]:

$$2ZnS + 3O_2 \rightarrow 2ZnO + 2SO_2 \tag{1}$$

To obtain detailed information about the structural properties of ZnS–ZnO films, crystallite size (D), dislocation density (δ) and micro strain ($<e>$) values were calculated. The equation given below was used to calculate the crystallite size values [35]:

$$D = \frac{K\lambda}{\beta cos\theta} \tag{2}$$

where K is constant, λ is the wavelength of the X-rays, β is half-peak width in radians for the respective crystal direction and θ is the Bragg's angle. Dislocation density (δ) was calculated using the expression determined by Williamson and Smallman [36].

$$\delta = \frac{n}{D^2} \tag{3}$$

where $n=1$ for the minimum δ value. Small δ values indicate that the crystallization level of the material is good [37]. The micro strain ($<e>$) values were calculated using the Eqs. (2) and (3) [38, 39]:

$$<e> = \frac{d - d_0}{d_0} \tag{4}$$

temperature, the dominant orientation of ZnS-525 films was found to be in the direction of the (002) ZnO plane at 34.79°. In addition, unlike other films, ZnO phases in the direction of (100), (101), and (004) planes were also detected in ZnS-525 films at 32.30°, 36.66° and 72.85°, respectively. Similar effects were also observed in the literature due to the loss of sulfur as a result of the oxidation process [29–33]. It is known that when

Table 1 Structural data for ZnS–ZnO films

Film	Observed		Standard		JCPDS Card No: ZnS-00-065-0723 ZnO-04-008-8196	
	2θ (°)	d (Å)	2θ (°)	d (Å)	(hkl)	Crystal System
ZnS	28.9833	3.0808	28.7690	3.1006	(111)	ZnS Cubic
ZnS-425	29.0202	3.0769	28.7690	3.1006	(111)	ZnS Cubic
	34.7291	2.5831	34.5520	2.5938	(002)	ZnO Hexagonal
ZnS-475	28.9838	3.0807	28.7690	3.1006	(111)	ZnS Cubic
	34.7376	2.5825	34.5520	2.5938	(002)	ZnO Hexagonal
ZnS-525	29.0017	3.0788	28.7690	3.1006	(111)	ZnS Cubic
	34.7926	2.5785	34.5520	2.5938	(002)	ZnO Hexagonal
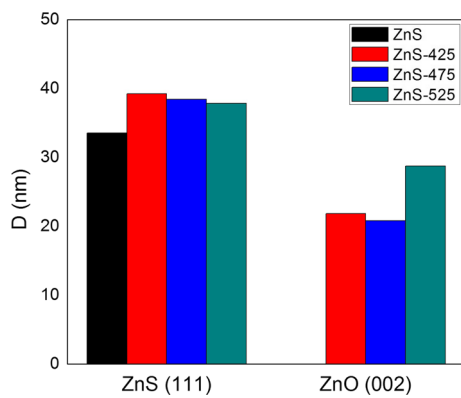
Fig. 2 Crystallite size for each phase in ZnS–ZnO films

Fig. 3 Change in relative intensity ratio $I_{(002)}/I_{(111)}$ for ZnS–ZnO films

where d_o and d are the distance between planes. The relative intensity ratio ($I_{(002)}/I_{(111)}$), crystallite size (D), dislocation density (δ) and micro strain ($<e>$) values calculated for ZnS–ZnO films are given in Table 2. Besides, negative macrostrain values for all films indicate the existence of shrinking planes in the crystal structure. This may be due to the difference in the coefficient of thermal expansion between the films and the substrate [40]. The crystallite size values for each phase are given in Fig. 2. The annealing process caused an increase in crystallite size value of ZnS phase. However, for ZnO phase, the highest crystallite size value was obtained for the annealing temperature of 525 °C. Figure 3 shows the variation of the relative intensity values calculated for the dominant orientations of the ZnS–ZnO films. Accordingly, it is clear that the (002) ZnO phase becomes more dominant as the annealing temperature increases.

3.2 Ellipsometric and optical analysis

The thicknesses of ZnS–ZnO films were determined by the spectroscopic ellipsometry technique. Ψ values were measured at 75° angle in the wavelength range of 1350–1450 nm and theoretical Ψ data were obtained by the Cauchy–Urbach model [41, 42]. ψ spectra of ZnS–ZnO films are given in Fig. 4. A good agreement was achieved between the
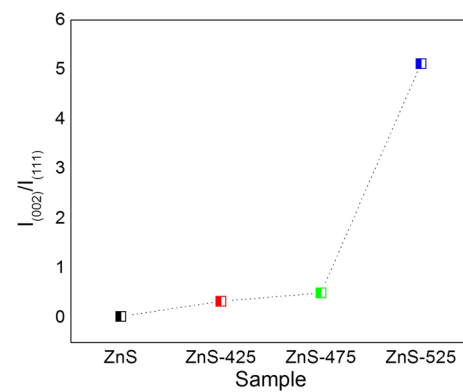
experimental and theoretical data. The source of minor deviations may be related to the physical parameters of the film (surface homogeneity, substrate used, depolarization effect, etc.). Parameters of the Cauchy–Urbach model and determined film thicknesses of ZnS–ZnO films are given in Table 3. As seen in Table 3, the thicknesses of the ZnS–ZnO films were determined to be in the range of 299–281 nm.

The refractive index (n) and extinction coefficient (k) spectra of ZnS–ZnO films determined using spectroscopic ellipsometry are given in Fig. 5. It is seen that the n values remain almost constant in the determined wavelength range. It is noteworthy that the refractive index value of the film annealed at the highest temperature (ZnS-525) decreases compared to other films. We think that this situation is related to the dominant ZnO phase in the structure as a result of the increase in annealing temperature. The extinction coefficient spectra of ZnS–ZnO films are given in Fig. 5b. The changes in k values of the films are similar and decrease as the wavelength increases.

The transmittance spectra of ZnS films are given in Fig. 6a. The annealing process at annealing temperatures of 425 °C and 475 °C did not cause a significant change in the transmittance values of the ZnS film. Except for sample ZnS-525, the transmittance values of other films are high (> 80%) at long wavelengths, and they behave as transparent materials, making them suitable materials for buffer layer

Table 2 The relative intensity ratio ($I_{(002)}/I_{(111)}$), crystallite size (D), dislocation density (δ) and micro strain ($<e>$) values of ZnS–ZnO films calculated from XRD data

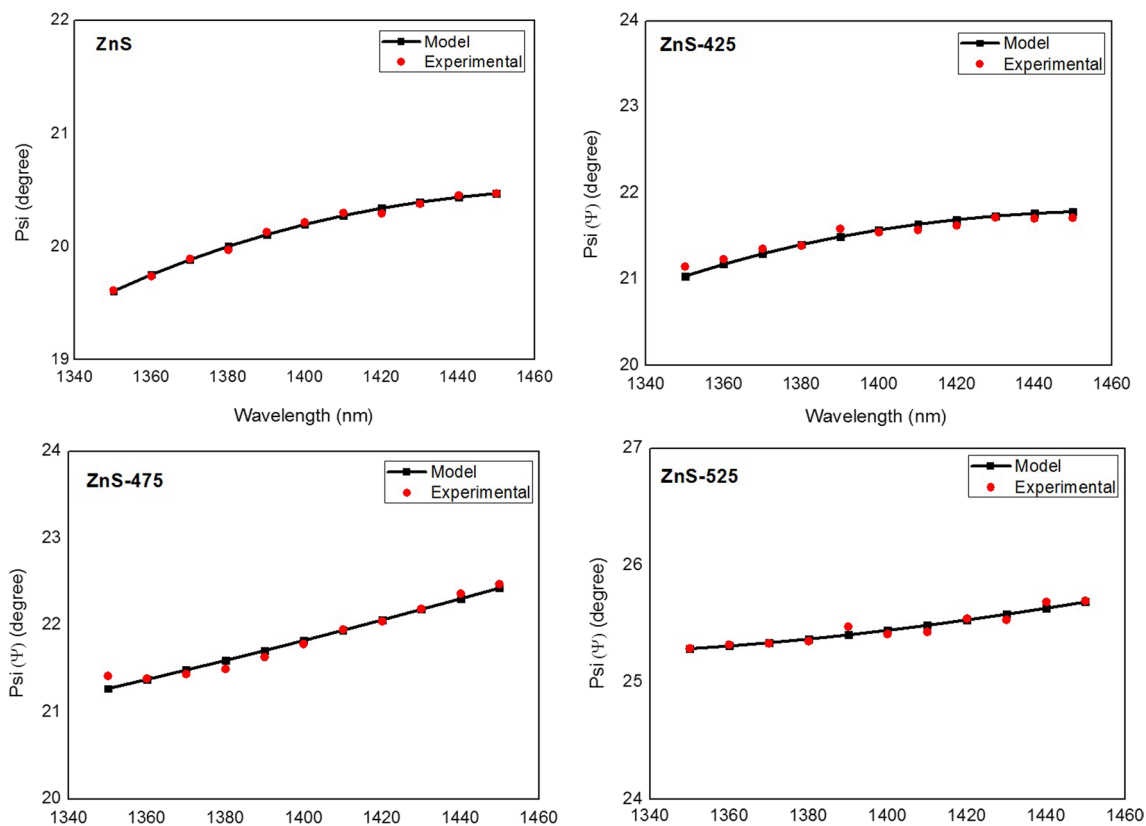| Film	Miller indices (hkl)	Relative intensity ratio $I_{(002)}/I_{(111)}$	D (nm)	δ (line/nm²)	$<e>$
ZnS	(111)-ZnS	–	33.55	8.88×10^{-4}	-6.38×10^{-3}
ZnS-425	(111)-ZnS	0.33	39.24	6.49×10^{-4}	-7.64×10^{-3}
	(002)-ZnO		21.83	2.11×10^{-3}	-4.12×10^{-3}
ZnS-475	(111)-ZnS	0.50	38.44	6.77×10^{-4}	-6.41×10^{-3}
	(002)-ZnO		20.83	2.34×10^{-3}	-4.35×10^{-3}
ZnS-525	(111)-ZnS	5.12	37.84	6.98×10^{-4}	-7.03×10^{-3}
	(002)-ZnO		28.77	1.21×10^{-3}	-5.89×10^{-2}

Fig. 4 Psi (ψ) spectra of ZnS–ZnO films

Table 3 Thickness and Cauchy–Urbach parameters for ZnS–ZnO films

Ellipsometric parameters	ZnS	ZnS-425	ZnS-475	ZnS-525
d (nm)	299	281	286	290
A_n	2.78	2.79	1.89	1.92
$B_n \times 10^{-2}$ $(nm)^2$	-3.41	-3.40	-0.02	-0.25
$C_n \times 10^{-2}$ $(nm)^4$	2.98	2.96	-0.27	-0.24
A_k	1.84	1.96	1.66	1.73
B_k $(eV)^{-1}$	1.05	10.2	1.05	1.05

applications in heterojunction solar cells. The interference fringes formed in the visible region in ZnS films started to lose their existence with the annealing process and they were completely removed by annealing at 525 °C. The absorption spectra of ZnS–ZnO films are given in Fig. 6b. For films annealed at 425 °C and 475 °C, the absorption values at long wavelengths appear to be the same as those of the sample ZnS. However, there is an increase in the absorption values of the ZnS-525 films. In addition to this increase in absorption, the annealing process caused the formation of a second absorption edge in the films. Especially, this change in the absorption edge became more distinct in ZnS film annealed at 525 °C. We think that this situation is caused by the ZnO

phase formed by the O atoms entering the structure of the films with the annealing process. In addition, reflectance spectra of ZnS–ZnO films are given in Fig. 6c. ZnS films have high reflectance values in the visible region and the annealing process caused a decrease in the reflectance values. This is an advantage for the ZnS–ZnO films, as it will prevent reflection losses that may occur in heterojunction solar cells. The decrease in the reflectance values may be due to surface properties such as grain boundaries, surface roughness, and morphology [43].

Optical band gap values of ZnS–ZnO films were calculated by the optical method [44]. Figure 7 and Table 4 show the $(\alpha h\nu)^2 \sim h\nu$ plots and the calculated band gap values for ZnS–ZnO films, respectively. As mentioned earlier, after the annealing process, the films have turned into a binary structure that includes the ZnS and ZnO phases together. This is also evident from the absorption and transmittance spectra. Therefore, there are two different band transitions for the films subjected to annealing process. Optical transitions corresponding to ZnS phase (E_{g1}) were changed between 3.55 and 3.31 eV. These values are in the appropriate range for buffer layers in heterojunction solar cells. In the literature, the band gap values of ZnS films were reported to change between 3.38 and 3.80 eV [45–49]. It was seen that the energy of the optical transitions for ZnS phase (E_{g1})
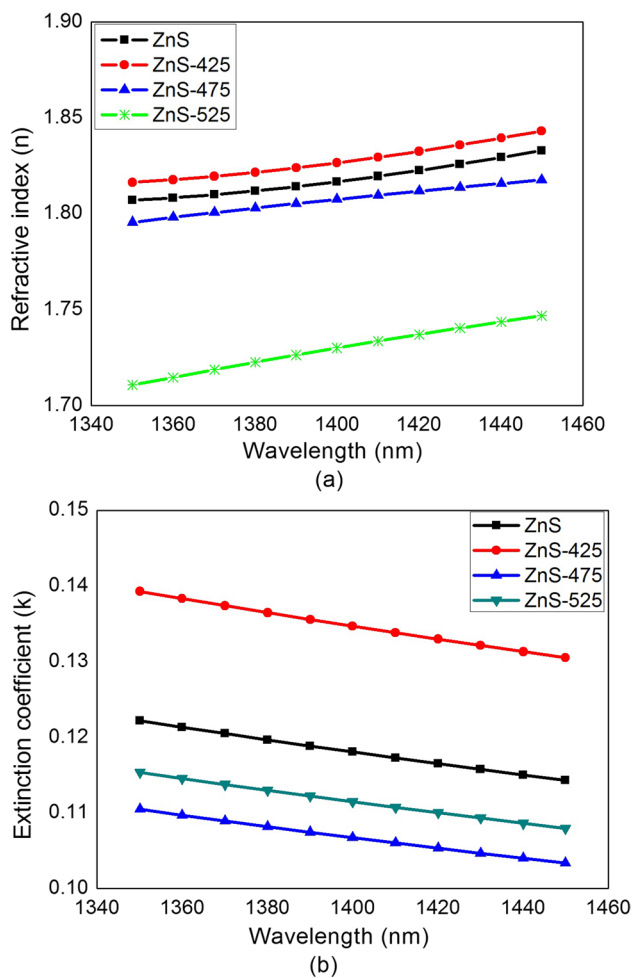
Fig. 5 a Refractive index spectra and **b** extinction coefficient spectra of ZnS–ZnO films

decreased with the effect of the annealing process, especially for ZnS-525 films annealed at 525 °C. This decrease may be due to the deformation created at the band edges by the oxygen atom entering the structure with the annealing process. The reduction of E_{g1} values with the annealing process will be appropriate in terms of increasing the photo-conversion efficiency of heterojunction solar cells [48]. Besides, as can be seen in Fig. 7 and Table 4, a second optical transition (E_{g2}) value for all annealed films was determined. E_{g2} values change between 3.20 and 3.22 eV with the increase in annealing temperature. We think that this optical transition is due to a second band related to the formation of ZnO phase after annealing, as supported by the XRD patterns.

Photoluminescence (PL) spectra of ZnS–ZnO films were taken to identify native point defects. PL measurements were performed at the emission wavelength range of 350–600 nm using an excitation wavelength of 325 nm. Figure 8 shows the PL spectra of the films. It was seen that films have unsymmetrical broad emission bands. In addition, it was
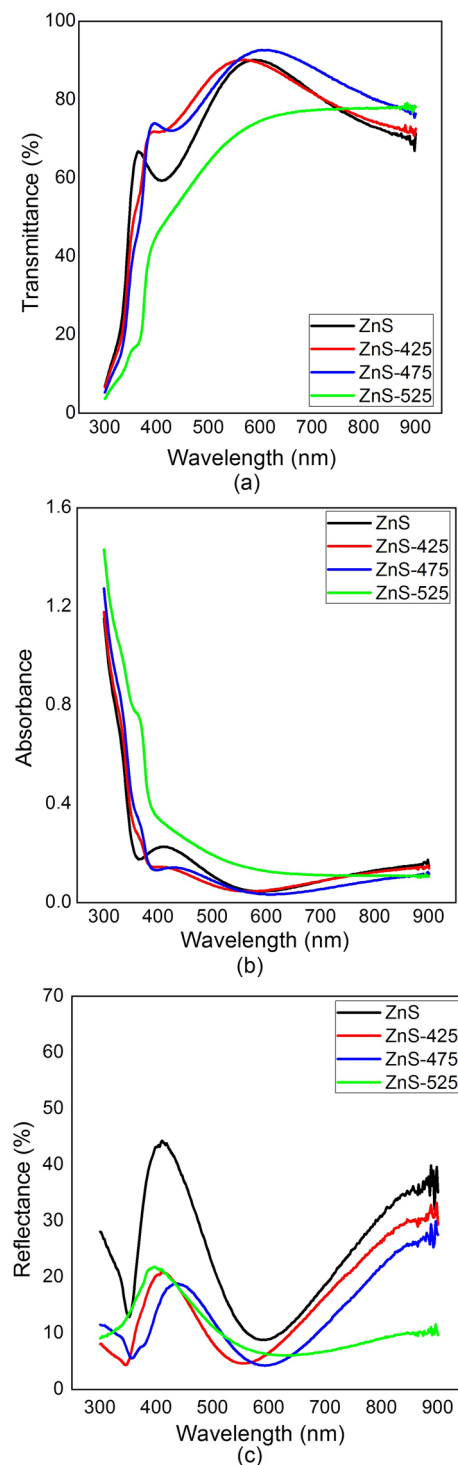

Fig. 6 a The transmittance, **b** absorbance and **c** reflectance spectra of ZnS–ZnO films

seen that the intensity of the peak with highest intensity decreased when compared to ZnS as a result of the reduction in electron–hole recombination rate. This refers an increase of available electron states in the conduction band, making

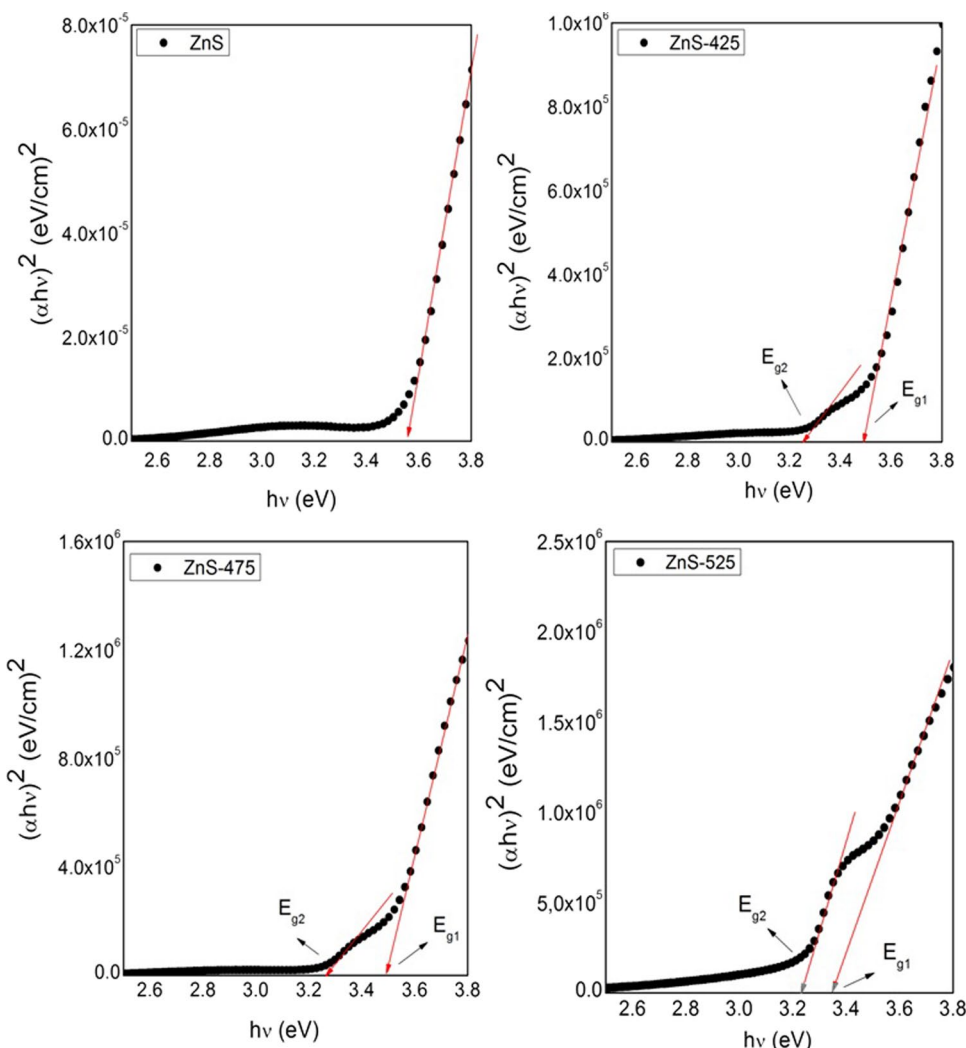**Fig. 7** $(\alpha h\nu)^2$ versus $h\nu$ plots of ZnS films

Table 4 The band gap values of ZnS–ZnO films

Optical transition	Energy of the optical transition (eV)			
	ZnS	ZnS-425	ZnS-475	ZnS-525
E_{g1}	3.55	3.51	3.49	3.31
E_{g2}	–	3.20	3.21	3.22

these films desirable candidates for solar cell applications. There are five emission peaks at 360 nm, 370 nm, 394 nm, 456 nm, and 485 nm for the films in Table 5. The peaks at 360 nm and 370 nm represent the near band edge emissions of ZnS [50]. The peaks in the wavelength range of 330–370 nm indicate band-to-band transitions for ZnS films [51]. Peaks between 380 and 400 nm, indicate purple emissions from bottom-level defects such as interstitial defects, dislocations, and Zn^{+2} in the structure [52]. The peaks between 430 and 470 nm are due to trapping states originating from surface states, Zn^{+2}, and S^{-2} holes [53]. These are the peaks caused by the deep and shallow traps formed under
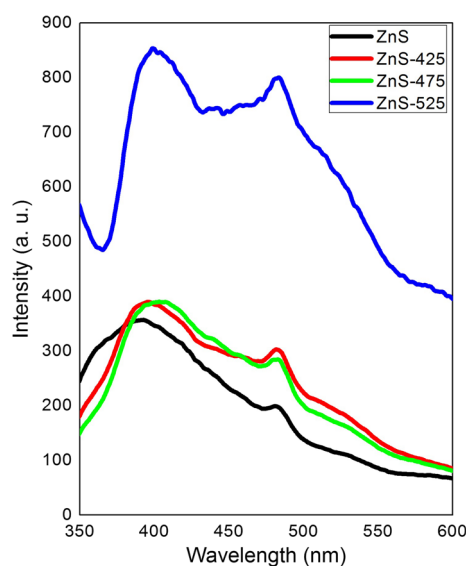

Fig. 8 PL spectra of ZnS films

Table 5 Emission peaks observed in the PL spectrum of ZnS films

Films	Peak 1		Peak 2		Peak 3		Peak 4		Peak 5	
	λ (nm)	E (eV)	λ (nm)	E (eV)	λ (nm)	E (eV)	λ (nm)	E (eV)	λ (nm)	E (eV)
ZnS	360	3.44	370	3.35	394	3.14	456	2.71	485	2.55
ZnS-425	–	–	–	–	395	3.13	456	2.71	485	2.50
ZnS-475	–	–	–	–	404	3.06	450	2.75	485	2.55
ZnS-525	–	–	–	–	404	3.06	406	3.05	485	2.55

the conduction band due to the surface defects in the structure [54, 55]. They are the peaks formed as a result of transitions from the energy level (V_s) formed by the sulfur vacancies in the structure to the valence band [54, 55]. As can be seen in Fig. 8, the emission peaks at 360 nm and 370 nm in ZnS films disappeared depending on the annealing process. The emission peaks at 394 nm shifted to long wavelengths, while the emission peaks at 456 nm shifted to short wavelengths. Besides, the intensity of the emission peaks at 394 nm and 456 nm increased as a result of oxidation. This increase may be related to the crystal structure of the films. Because the increase in the crystallite size may lead to a decrease in the defects (Table 2). Besides, a new peak formation was detected at 406 nm for ZnS-525 films annealed at high temperatures. The shift in the emission peaks in the annealed films and this newly formed peak is due to the ZnO phase observed in the crystal structure as a result of O entering the structure with the annealing process. Especially in

the ZnS-525 film, the emission peaks at 404–406 nm can be called the band-edge emission of ZnO [56].

3.3 Morphological analysis

Surface morphologies of the films were examined using atomic force microscope (AFM) and field emission scanning electron microscope (FESEM). As seen in Fig. 9, the annealing process at different temperatures caused a significant change in the surface texture of the films. ZnS film has a homogeneous, distinguishable and needle-like surface structure. The needle-type surface structure was completely lost as a result of the annealing process. The large clusters formed by the effect of the annealing process changed the distribution on the surface causing the homogeneity to deteriorate. R_q (rms) and R_a (average) roughness values of the films are given in Table 6. It is noteworthy that the surface roughness values of the ZnS film are lower
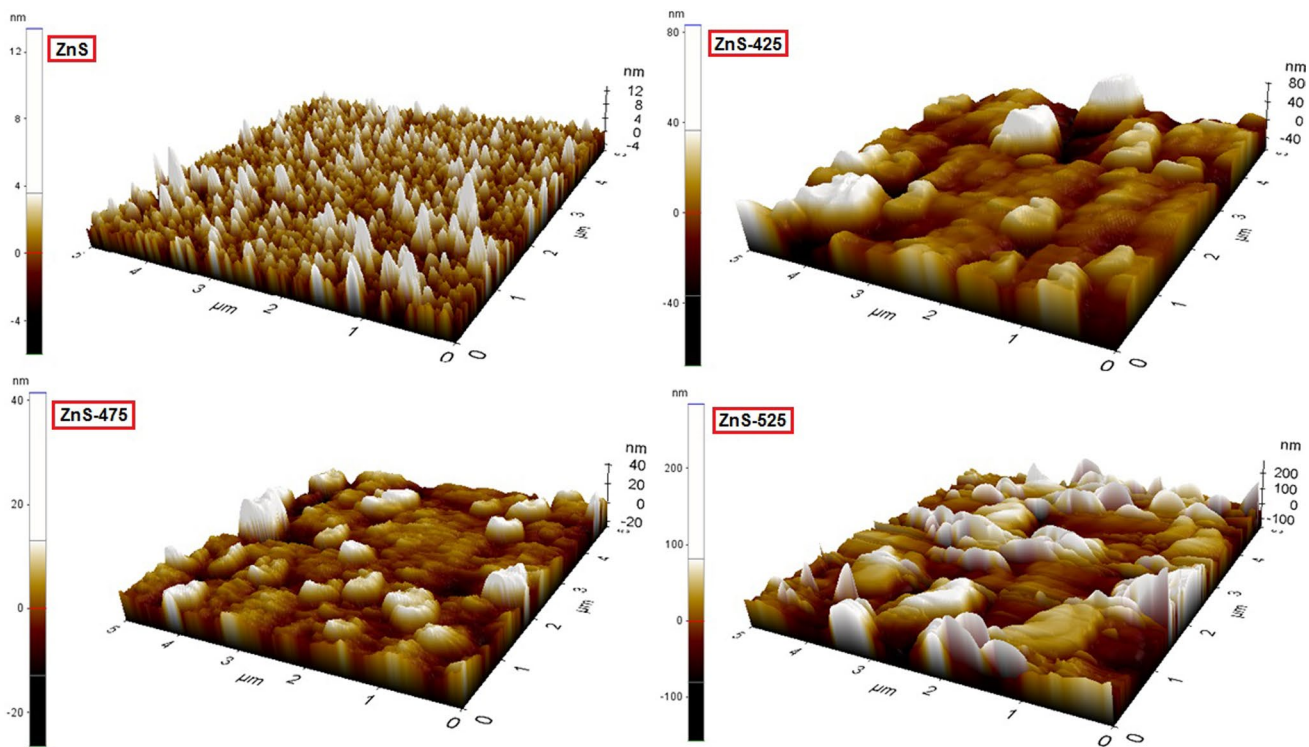

Fig. 9 AFM surface images of the films

Table 6 Roughness values of the films

Film	R_q (nm)	R_a (nm)
ZnS	2	1
ZnS-425	19	13
ZnS-475	7	5
ZnS-525	41	31

than those of the annealed films. We think that this may be due to the loss of sulfur and partial oxidation mechanisms on the surface.

FESEM images, EDX spectra and atomic percentage values for the films are given in Fig. 10. Similar to AFM results, FESEM images shows that annealing process caused the surface texture of the ZnS films to change significantly. For ZnS films, it is seen that a tight structuring occurs due to uniformly distributed particles on the surface. For especially ZnS-425 and ZnS-475 films, the annealing process caused the particle sizes and cracks to increase. The disappearance of cracks in ZnS-525 films is important in terms of photovoltaic applications. However, agglomerations were formed on the surface with the effect of the annealing process, as supported by the AFM images. EDX results in Fig. 10 show that Zn and S elements are present in ZnS films, and the Zn atomic percentage is higher than that of S. EDX analysis also supports that oxygen joins the structure with the effect of the annealing process and accordingly, the atomic ratio of sulfur decreases. The loss of S not only affected the composition of the films, but also caused significant changes in the crystal structure, leading to the formation of the ZnO phase, as supported in the literature [49, 57]. This refers that the ZnS phase can be transformed into ZnS–ZnO binary structure, as supported by XRD results.

3.4 Electrical analysis

One of the most important parameters determining the potential of the produced films in solar cell applications is their electrical properties. In this study, the two-probe technique was used to determine the electrical resistivity values of the films. I-V plots of the films are given in Fig. 11. The annealing process caused a significant change in the resistivity values of the ZnS films. The resistivity values of ZnS, ZnS-425, ZnS-475 and ZnS-525 films were found as 1.28×10^5, 6.89×10^2, 2.89×10^2, and 3.84×10^1 Ωcm respectively. While the resistivity of ZnS films was in the order of 10^5, those of the annealed films decreased up to the order of 10^2 and 10^1. We think that the formation of ZnO phase with the annealing process in ZnS–ZnO films caused a decrease in resistivity values of the films. Besides, the determined resistivity values are suitable for the use of the films as a buffer layer in solar cells.

4 Conclusions

ZnS–ZnO binary films as an alternative buffer layer were produced by thermal evaporation, a technique that is easy to apply for large surfaces and allows the production of materials with the desired thickness. As a result of annealing at high temperatures (> 500 °C); ZnS–ZnO binary structure was obtained by ensuring the formation of ZnO phase in the ZnS structure. The films with ZnS–ZnO binary structure have different optical properties and dual band structure. The surface roughness values of the films were increased compared to those of ZnS films; thus high roughness values (31 nm) were achieved in the absorber layers. A new emission peak at 406 nm was detected for ZnS–ZnO binary films. Compared to the resistivity of the pure ZnS film (1.28×10^5 Ω cm), films with ZnS–ZnO binary structures (3.84×10^1 Ω cm) were obtained with much lower resistivity values. It has been deduced that ZnS–ZnO films obtained at 525 °C have the potential to replace ZnS films as buffer layers due to their increased absorbance, conductivity, and roughness values.
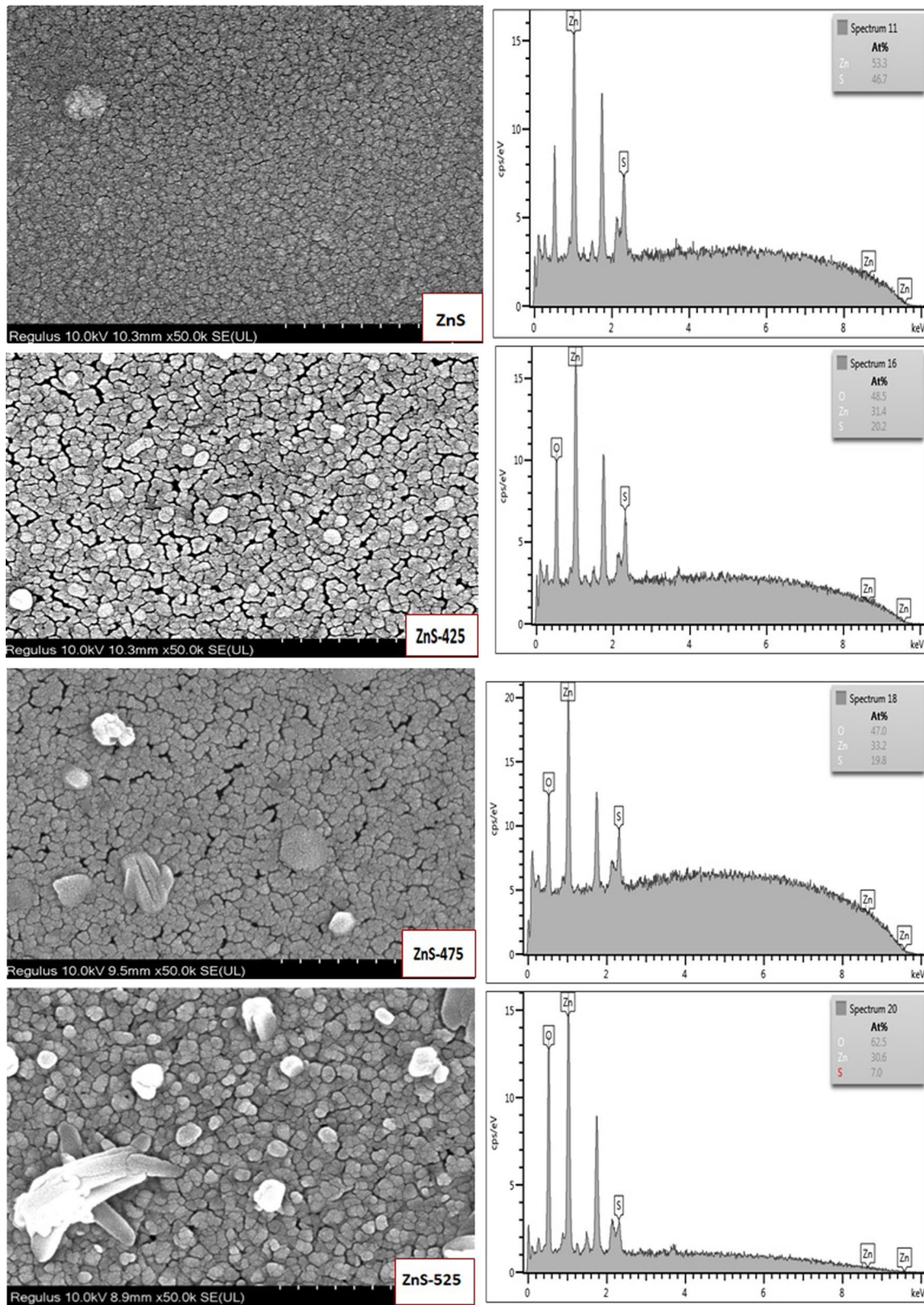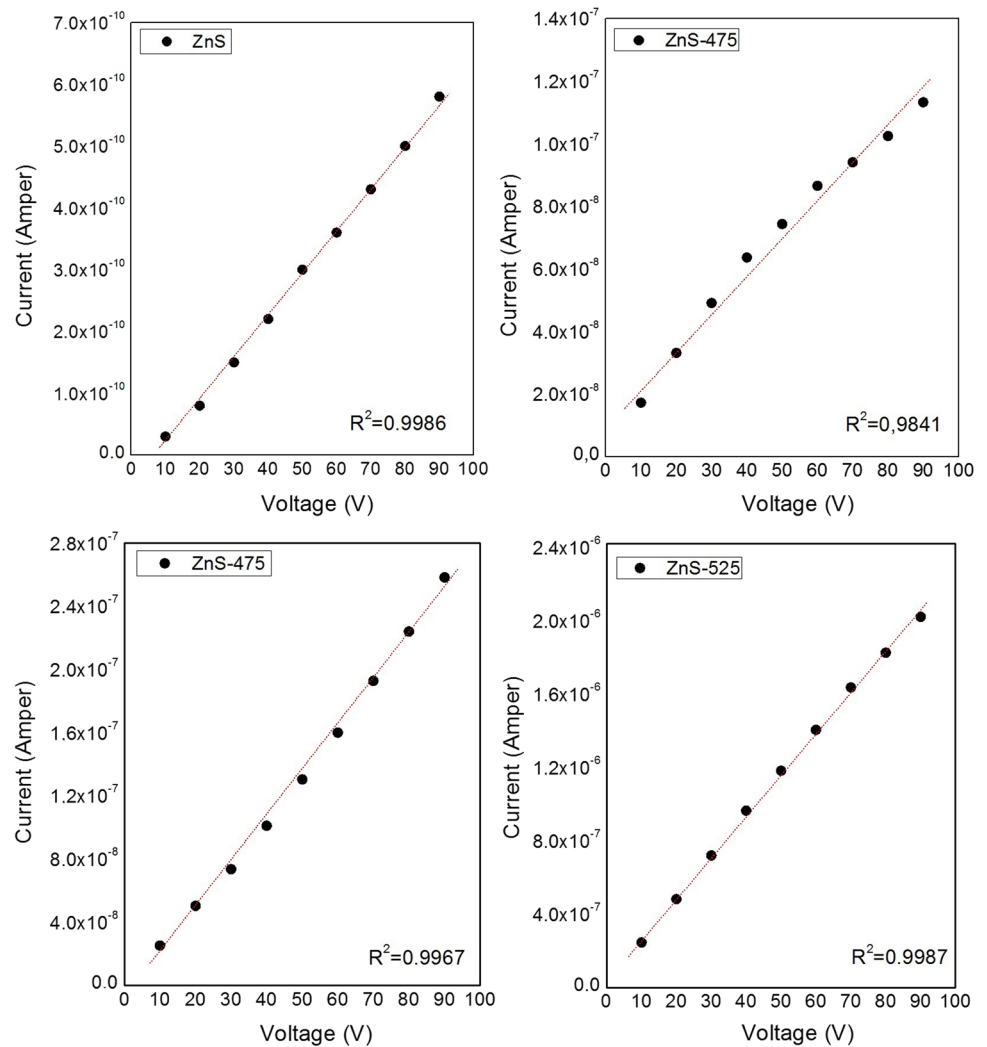
Fig. 10 FESEM images, EDX spectra and atomic ratio for the films

Fig. 11 Current–voltage (I–V) plots of ZnS films

Declarations

Conflict of interest The authors declare that they have no conflict of interest.

References

1. E. Akman, S. Akin, G. Karanfil, S. Sönmezoğlu, Organik Güneş Pilleri. Trakya Univ J Sci **14**(1), 1–30 (2013)
2. A. Cantas, F. Turkoglu, E. Meric, F.G. Akca, M. Ozdemir, E. Tarhan, L. Ozyuzer, G. Aygun, Importance of CdS buffer layer thickness on Cu2ZnSnS4-based solar cell efficiency. J. Phys. D Appl. Phys. **51**, 275501 (2018)
3. O.K. Echendu, A.R. Weerasinghe, D.G. Diso, F. Fauzi, I.M. Dharmadasa, J. Electron. Mater. **42**, 692–700 (2013)

4. R. Mahbub, M.S. Islam, F. Anwar, S.S. Satter, S.M. Ullah, Simulation of CZTS thin film solar cell for different buffer layers for high efficiency performance. South Asian Res. J. Eng. Tech. **2**, 1–10 (2016)

5. J.B. Varley, V. Lordi, Electrical properties of point defects in CdS and ZnS. Appl. Phys. Lett. **103**, 4 (2013)

6. V. Dimitrova, J. Tate, Synthesis and characterization of some ZnS-based thin film phosphors for electroluminescent device applications. Thin Solid Films **365**, 134–138 (2000)

7. L.-X. Shao, K.-H. Chang, H.-L. Hwang, Zinc sulfide thin films deposited by RF reactive sputtering for photovoltaic applications. Appl. Surf. Sci. **212**, 305–310 (2003)

8. W. Witte, S. Spiering, D. Hariskos, Substitution of the CdS buffer layer in CIGS thin-film solar cells. Dunne Schicht. **26**, 23–27 (2014)

9. C.-H. Lai, Lu. Ming-Yen, L.-J. Chen, Metal sulfide nanostructures: synthesis, properties and applications in energy conversion and storage. J. Mater. Chem. **22**, 19–30 (2012)

10. C.-Y. Yeh, Z.W. Lu, S. Froyen, A. Zunger, Zinc blende—wurtzite polytypism in semiconductors. Phys. Rev. B **46**, 10086–10097 (1992)

11. A.R.M. Razeghi, Semiconductor ultraviolet detectors. Appl. Phys. Rev. **79**(10), 7433 (1996)

12. M. Zahan, M.R. Islam, J. Podder, Influence of annealing temperature on tuning the band gap of Mn-doped ZnS thinfilms deposited by spray pyrolysis technique. Indian J. Phys. **93**, 611–616 (2019)

13. R. Hernández Castilloa, M. Acostaa, I. Riecha, G. Santana-Rodríguez, J. Mendez-Gamboaa, C. Acostaa, M. Zambrano, Study of ZnS/CdS structures for solar cells applications. Optik **148**, 95–100 (2017)

14. F. Haque, N.A. Khan, K.S. Rahman, M.A. Islam, M. M. Alam, K. Sopian, N.Amin, Prospects of zinc sulphide as an alternative buffer layer for CZTS solar cells from numerical analysis, in *8th International Conference on Electrical and Computer Engineering 20–22 December, Dhaka* (2014)

15. C. Wang, Fabrication and optical-electrical characteristics of ZnS/ZnO films by pulsed laser deposition. Thin Solid Film **7800**, 139971 (2023)

16. P. Banerjee, Impact of thermally grown $ZnS_{1-x}O_x$ buffer layer over the photovoltaic performance of SnS/ZnS heterostructure. Mater. Lett. **320**, 132347 (2022)

17. K. Deepaa, K.C. Preetha, K.V. Murali, A.C. Dhanya, A.J. Ragina, T.L. Remadevi, The effect of various complexing agents on the morphology and optoelectronic properties of chemically deposited ZnS thin films: a comparative study. Optik **125**, 5727–5732 (2014)

18. S. Serkis-Yesilkaya, U. Ulutas, Influence of indium on the parameters of ZnS thin films and $ZnS/CuInS_2$ cells. Mater. Lett. **315**, 131959 (2022)

19. A. Sundhar, Development of ZnS thin film with Co, Cu and Ag doping using SILAR method. Mater. Today Proc. **48**, 377–381 (2022)

20. M. Saglam, B. Güzeldir, Time-dependent of characteristics of Cu/CuS/n-GaAs/In structure produced by SILAR method. Mater. Res. Bull. **81**, 55–62 (2016)

21. M.M. El-Desoky, G.A. El-Barbary, D.E. El Refaey, F. El-Tantawy, Optical constants and dispersion parameters of La-doped ZnS nanocrystalline films prepared by sol–gel technique. Optik **168**, 764–777 (2018)

22. I.Y.Y. Bu, Sol–gel synthesis of ZnS (O, OH) thin films: Influence of precursor and process temperature on its optoelectronic properties. J. Lumin. **134**, 423–428 (2013)

23. K. Priya, V.K. Ashith, G.K. Rao, G. Sanjeev, A comparative study of structural, optical and electrical properties of ZnS thin films obtained by thermal evaporation and SILAR techniques. Ceram. Int. **43**, 10487–10493 (2017)

24. W.-S. Liu, C.-S. Huang, S.-Y. Chen, M.-Y. Lee, H.-C. Kuo, Investigation of Cu_2ZnSnS_4 thin film with preannealing process and ZnS buffer layer prepared by magnetron sputtering deposition. J. Alloy. Compd. **884**, 161015 (2021)

25. J. Koskinen, Cathodic-arc and thermal-evaporation deposition. Compr. Mater. Process. **4**, 3–55 (2014)

26. E.M. Flores, C.W. Raubach, R. Gouvea, E. Longo, S. Cava, M.L. Moreira, Optical and structural investigation of ZnO@ ZnS core-shell nanostructures. Mater. Chem. Phys. **173**, 347–354 (2016)

27. C.D. Fernandes, M.M. Ferrer, C.W. Raubach, E.C. Moreira, L.T. Gularte, S. Cava, M.J. Piotrowski, P.L.G. Jardim, R.D. Carvalho, M.L. Moreira, An investigation of the photovoltaic parameters of ZnS grown on ZnO (101). New J. Chem. **44**(47), 20600–20609 (2020)

28. E.M. Flores, R.A. Gouvea, M.J. Piotrowskia, M.L. Moreira, Band alignment and charge transfer predictions of ZnO/ZnX (X= S, Se or Te) interfaces applied to solar cells: a PBE+ U theoretical study. Phys. Chem. Chem. Phys. **20**(7), 4953–4961 (2018)

29. T. Dedova, M. Krunks, O. Volobujeva, I. Oja, ZnS thin films deposited by spray pyrolysis technique. Phys. Status Solidi C **2**, 1161–1166 (2005)

30. M.S. Akhtar, M.A. Malik, S. Riaz, S. Naseem, P. O'Brien, Optimising conditions for the growth of nanocrystalline ZnS thin films from acidic chemical baths. Mater. Sci. Semicond. Process. **30**, 292–297 (2015)

31. T. Liu, Y. Li, H. Ke, Y. Qian, S. Duo, Y. Hong, X. Sun, Chemical bath co–deposited ZnS film prepared from different zinc salts: $ZnSO4$–$Zn(CH3COO)_2$, $Zn(NO_3)_2$–$Zn(CH_3COO)_2$, or $ZnSO_4$–$Zn(NO_3)_2$. J. Mater. Sci. Technol. **32**, 207–217 (2015)

32. Y.F. Nicolau, J.C. Menard, Solution growth of ZnS, CdS and Zn1−xCdxS thin films by the successive ionic layer adsorption and reaction process; growth mechanism. J. Cryst. Growth **92**, 128–142 (1988)

33. O. Ozakın, B. Guzeldir, M.A. Yıldırım, M. Saglam, A. Ates, Influence of film thickness on structural and optical properties of ZnS thin films obtained by SILAR method and analysis of Zn/ZnS/n-GaAs/In sandwich structure. Phys. Status Solidi A **209**, 687–693 (2012)

34. R. Wahab, S.G. Ansari, Y.-S. Kim, M.S. Dhage, H.K. Seo, M. Song, H.-S. Shin, Effect of annealing on the conversion of ZnS to ZnO nanoparticles synthesized by the sol-gel method using zinc acetate and thiourea met. Mater. Int. **15**(3), 453–458 (2009)

35. A.L. Patterson, The Scherrer formula for X-ray particle size determination. Phys. Rev. **56**(10), 978–982 (1939)

36. Z. Zhao, D.L. Morel, C.S. Ferekides, Electrical and optical properties of thin-doped CdO films deposited by atmospheric metalorganic chemical vapour deposition. Thin Solid Films **413**, 203–211 (2002)

37. B.D. Cullity, S.R. Stock, *Elements of X-ray Diffraction*, 3rd edn. (Prentice Hall, Hoboken, 2001)

38. K. Priya, G.K. Rao, V.K. Ashith, G. Sanjeev, V.P. Verma, V.C. Petwal, J. Dwivedi, The effect of 8 MeV electron beam irradiation on the structural, optical and photoluminescence properties of ZnS thin films. Ceram. Int. **45**, 2575–2583 (2019)

39. İ. Akyüz, CdO Filmlerinin bazı fiziksel özellikleri üzerine Al katkılama ve tavlama işlemlerinin etkileri, Doktora tezi, Eskişehir Osmangazi Üniversitesi Fen Bilimleri Enstitüsü, 119 s (2005)

40. H. Ennaceri, M. Boujnah, D. Erfurt, J. Rappich, Xi. Lifei, A. Khaldoun, A. Benyoussef, A. Ennaoui, A. Tale, Influence of stress on the photocatalytic properties of sprayed ZnO thin films. Sol. Energy Mater. Sol. Cells **201**, 110058 (2019)

41. Y. Yang, X.W. Sun, B.J. Chen, C.X. Xu, T.P. Chen, C.Q. Sun, B.K. Tay, Z. Sun, Refractive indices of textured indium tin oxide and zinc oxide thin films. Thin Solid Films **510**(1–2), 95–101 (2006)

42. F.K. Shan, Z.F. Liu, G.X. Liu, B.C. Shin, Y.S. Yu, S.Y. Kim, T.S. Kim, Spectroscopic ellipsometry characterization of Al-doped

ZnO thin films deposited by pulsed laser deposition. J Korean Phy. Soc **44**(5), 1215–1219 (2004)

43. J. Vidal, O. de Melo, O. Vigil, N. Lopez, G. Contreras-Puente, O. Zelaya-Angel, Influence of magnetic field and type of substrate on the growth of ZnS films by chemical bath. Thin Solid Films **419**, 118–123 (2002)

44. J.I. Pankove, *Optical Processes in Semiconductors* (Dover Publication Institute, New York, 1971), p.422

45. J. Kennedy, P.P. Murmu, P.S. Gupta, D.A. Carder, S.V. Chong, J. Leveneur, S. Rubanov, Effects of annealing on the structural and optical properties of zinc sulfide thin films deposited by ion beam sputtering. Mater. Sci. Semicond. Process. **26**(561–566), 44 (2014)

46. H. Ahn, Y. Um, Post-annealing effects on ZnS thin films grown by using the CBD method. J. Korean Phys. Soc. **67**(6), 1045–1050 (2015)

47. M. Asghar, K.B.S. Mahmood, S. Rabia, M. Shahid, Effect of annealing temperature on the structural and optical properties of ZnS thin films. Mater. Today Proc. **2**, 5430–5435 (2015)

48. S. Kannan, N.P. Subiramaniyam, M. Sathishkumar, Inorg. Chem. Commun. **119**, 108068 (2020)

49. A. Kumar, M. Kumar, V. Bhaat, D. Kim, S. Mukherjee, Chem. Phys. Lett. **763**, 138162 (2021)

50. M.V. Limaye, S. Gokhale, S.A. Acharya, S.K. Kulkarni, Template-free ZnS nanorod synthesis by microwave irradiation. Nanotechnology **19**, 41 (2008)

51. Y. Chang, M. Wang, X. Chen, S. Ni, W. Qiang, Solid State Commun. **142**, 295 (2007)

52. W.G. Becker, A.J. Bard, J. Phys. Chem-US **87**, 4888 (1983)

53. A.A. Bol, A. Meijerink, J. Phys. Chem-B **108**, 10203 (2001)

54. M. Sookhakian, Y.M. Amin, W.J. Basirun, M.T. Tajabadi, N. Kamalrulzaman, J. Lumin. **145**, 244–252 (2014)

55. B. Demirselcuk, E. Kus, A. Kucukarslan, E. Sarica, I. Akyuz, V. Bilgin, Optimization of chemically sprayed ZnS films by Mn doping. Phys. B Phys. Condens. Matter **622**, 413353 (2021)

56. X. Chen, W. Liu, G. Zhang, N. Wu, L. Shi, S. Pan, Efficient photoluminescence of Mn^{2+}-doped ZNS quantum dots sensitized by hypocrellin A, Adv. Mater. Sci. Eng. Article ID 412476, 8 (2015)

57. I.Y.Y. Bu, J. Lumin. **133**, 423–428 (2013)